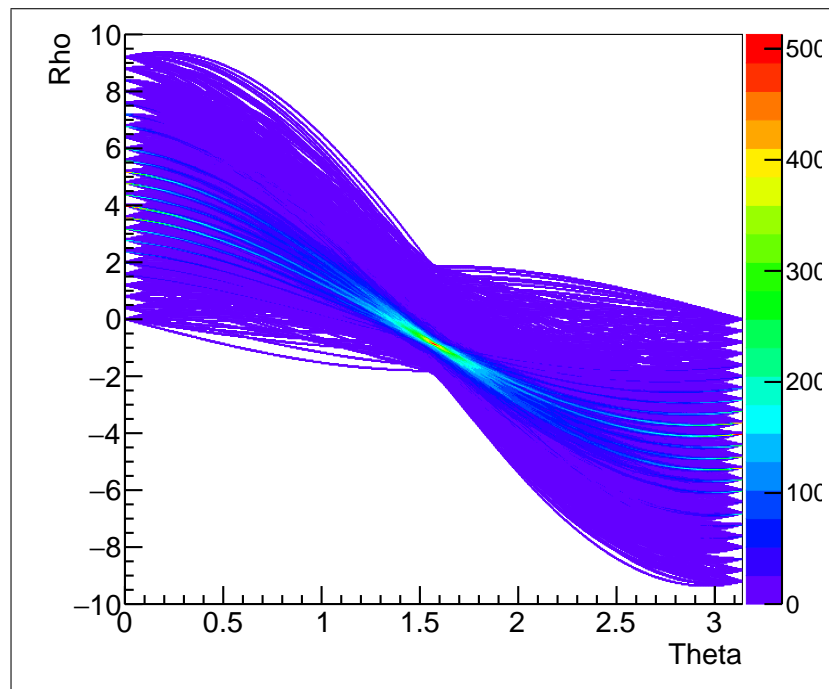**Universiteit Utrecht**

Opleiding Natuur- en Sterrenkunde

Data analysis of FoCal at 244 GeV using the Hough transform and longitudinal profiles

BACHELOR THESIS

Thomas Mons

Supervisors:

Dr. ir. G.J.L. Nooren
University Utrecht

Prof. Dr. T. Peitzmann
University Utrecht

14-6-2017

Abstract

The FoCal prototype detector is a prototype digital sampling calorimeter. In 2014 data was taken from the SPS accelerator at CERN at 244 GeV, consisting of electrons, positrons and hadrons. This thesis analyses that data. By looking at the longitudinal profiles of events, it is concluded that the length of a shower can be used to distinguish between partial and full showers. The Hough transform is used to find the position of incoming particles, it is not succesful in finding secondary tracks.

Contents

Chapter 1

Introduction

The FoCal (forward calorimetry) detector is a proposed detector to be placed in the forward direction at the ALICE (a large ion collider experiment) detector at CERN. The goal of ALICE is to study the quark gluon plasma (QGP), which will give us information about the very early stages of the universe. The FoCal detecor will measure the energy of photons exiting the collisions under a small angle. It is important to be able to distinguish between incoming particles that are close together. In particular, we would like to distinguish between the two photons produced by the decay of neutral pions. This is where the digital calorimeter can be very useful. In this thesis I will try to develop a method to find primary and secondary tracks with the Hough transform. I will also look at the longitudinal profile of events to distinguish between different types of incoming particles i.e. hadrons and electrons. The data used for this thesis is the 244 GeV data taken at the SPS accelerator at CERN in 2014.

I will start by explaining the underlying physical processes in this detector as well as the mathematical methods used in the analysis in chapter 2. Then I will describe the design of the detector in chapter 3. In chapter 4 I will describe the processing of data prior to analysis. In chapter 5 all data analysis I have done will be discussed. Lastly I will finish with a conclusion reiterating the most important findings and containing recommendations for further research.

Chapter 2

Theory

The goal of this chapter is to explain the physical concepts which are necessary to understand the functioning of the FoCal detector. The Hough transform is also explained as it is used for the data analysis.

2.1 Interactions with matter

This section will explain the way particles interact with matter and give a general description of particle showers.

2.1.1 Bremsstrahlung

As visible in figure 2.1, bremsstrahlung becomes the dominant process for energy loss for electrons and positrons passing through matter at an energy of ≈ 7 MeV. Since this thesis only works with incoming particles with an energy of 244 GeV, bremsstrahlung is the dominant process in the detector for the first interactions. Bremsstrahlung is caused by charged particles approaching a nucleus. The particle is then deflected by the nucleus and emits a photon. The formula for the radiated power of the bremsstrahlung is as follows:

FIGURE 2.2: Feynman diagram of bremsstrahlung

$$P = \frac{q^2\gamma^4}{6\pi\epsilon_0 c}(\dot{\beta} + \frac{\vec{\beta} \cdot \vec{\beta}}{1 - \beta^2}) = \frac{q^2\gamma^6}{6\pi\epsilon_0 c}(\dot{\beta} - (\vec{\beta} \times \vec{\beta})^2), \tag{2.1}$$

with P the radiated power, q the charge of the particle, γ the Lorentz factor, ϵ_0 the electric constant and $\beta = \frac{v}{c}$ the speed of the particle as a fraction of the light speed.
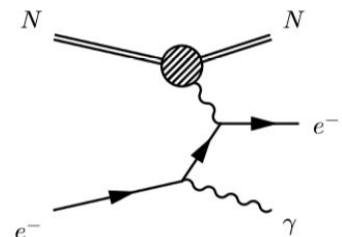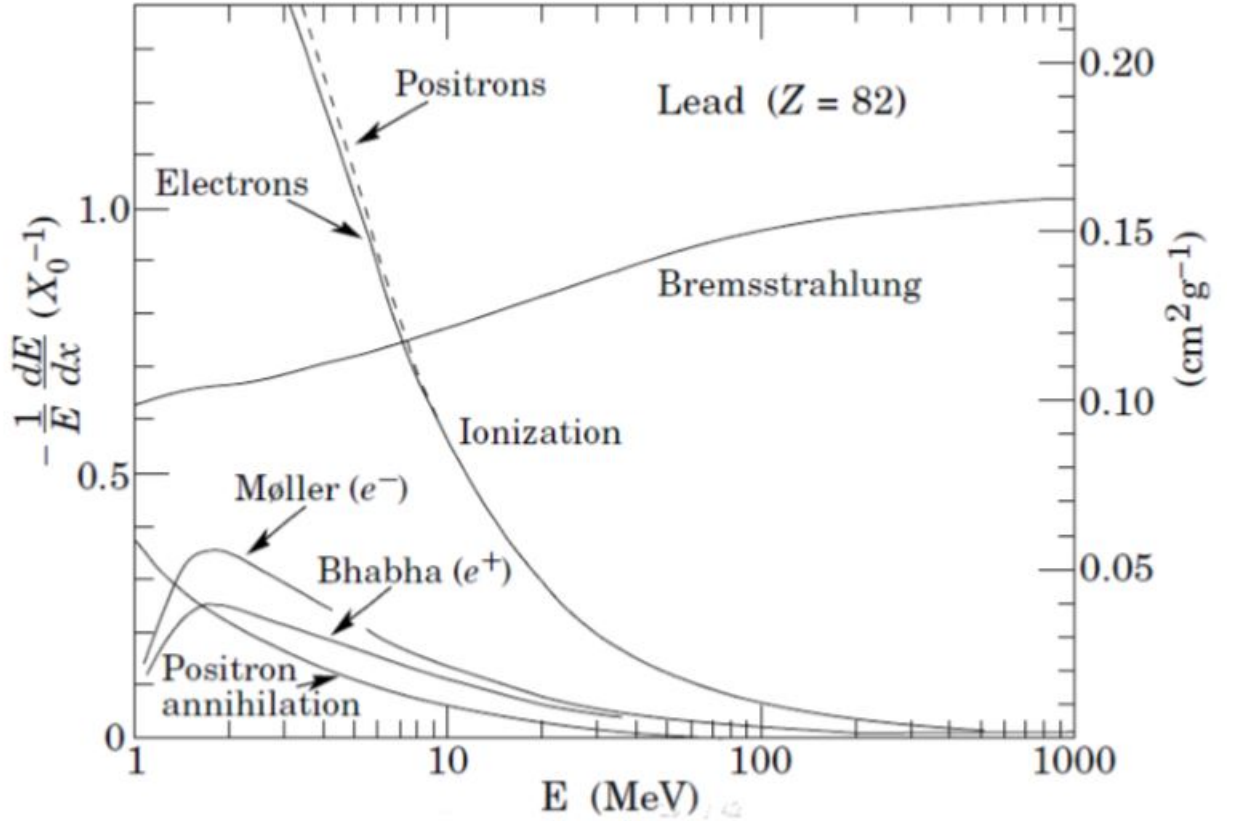
FIGURE 2.1: The processes of energy loss for electrons and positrons [1]

The angular distribution of bremsstrahlung is as follows:

$$\frac{dP}{d\Omega} = \frac{q^2}{16\pi^2\epsilon_0 c} \frac{|\hat{n} \times ((\hat{n} - \vec{\beta}) \times \dot{\vec{\beta}})|^2}{(1 - \hat{n} \cdot \vec{\beta})^5},$$ (2.2)

where $d\Omega$ is an infinitesimal amount of angle and $\hat{n}$ is the unit vector from the particle to the observer. Because of the $(1 - \hat{n} \cdot \vec{\beta})^5$ term the radiation is strongly concentrated in the travel direction of the original particle. This concentration becomes higher at higher speeds. This explains why electromagnetic showers are very narrow events compared to hadronic showers.

2.1.2 Ionization

When charged particles pass through matter, they lose energy via ionization. In the process of ionization incoming particles collide with electrons in the material via the Coulomb interaction. This leads to atoms in the material being excited or ionized. The incoming particle is slowed down, and scattered. Since electrons and positrons are much lighter than hadrons they scatter more. The energy loss for ionization is given by the
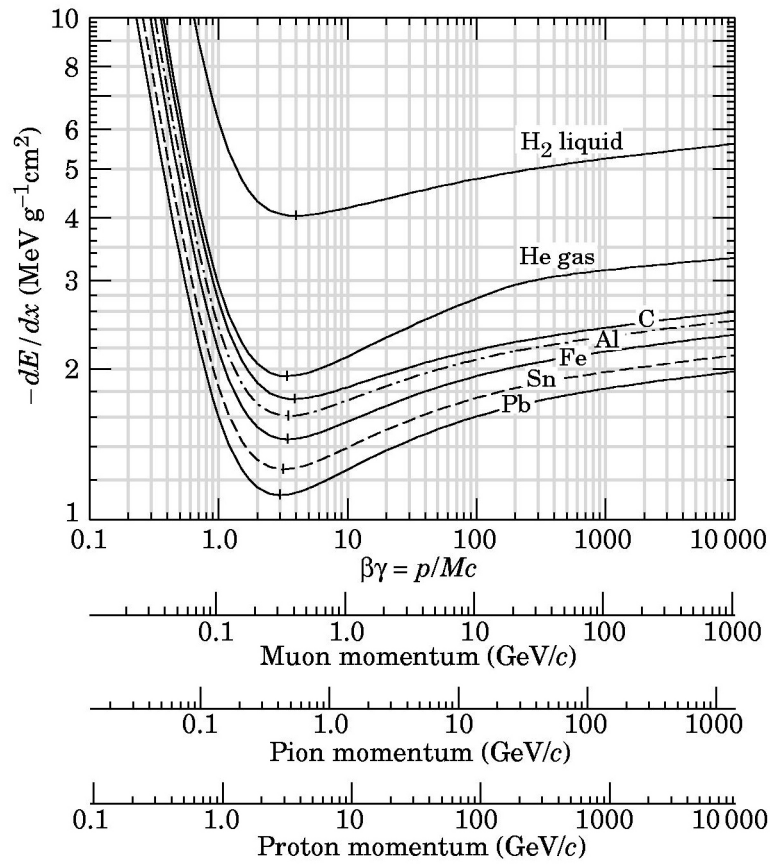
FIGURE 2.3: The energy loss due to ionization in some materials according to the Bethe-Bloch formula[2]

Bethe-Bloch formula:

$$-\frac{dE}{dx} = \frac{4\pi n z^2 Z^2 e^4}{m_e v^2}(\ln \frac{2m_e v^2}{I(1-\beta^2)} - \beta^2).\qquad(2.3)$$

Here $\frac{-dE}{dx}$ is the energy loss per distance, n the number of electrons per cm^3, Z the atomic number of the stopping material, m_e the electron mass, z the charge of the particle, v the speed of the particle, β the speed relative to the speed of light and I the mean excitation potential of the atoms of the stopping material. In figure 2.3 this is displayed for multiple materials, with a different scale per incoming particle mass. The minimum of the function gives a particle energy that hardly interacts with the material. We call these particles minimum ionizing particles (MIP's). The hadrons in this thesis have a higher energy than that minimum, but still do not ionize easily. Electrons and positrons mainly lose energy via ionization when they are under the critical energy of ≈ 7 MeV, as visible in figure 2.1.

2.1.3 Pair production

The photons that are produced by e.g. bremsstrahlung can interact with the material via pair production. Pair production is the dominant interaction process at energies much higher than the rest mass of the electron ($m \approx 0.51\text{MeV}/c^2$), which is the case for most interactions in this thesis. In pair production a photon converts into an electron-positron pair in the electric field of a nearby nucleus. Note that the energy of the incoming photon has to be at least twice the electron mass, otherwise it is impossible to produce an electron-positron pair. The positron and electron will then continue trough the material. At low enough energies the positron will annihilate with a nearby electron, producing two photons.
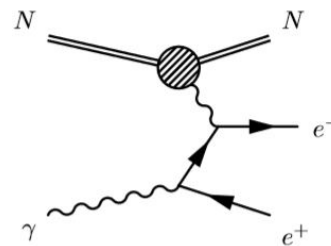

FIGURE 2.4: Feynman diagram of pair production

2.1.4 Cherenkov radiation

Cherenkov radiation are photons that are emitted from a particle that is travelling through a medium at a speed faster than the phase velocity of light in the medium. It is important here to distinguish between phase velocity and group velocity. The group velocity is the velocity at which the overall shape or modulation of a wave travels, whereas the phase velocity is the velocity of the phase of a wave. So even though a particle cannot travel faster than group velocity of light in vacuum, it can travel faster than the phase velocity in the medium. Somewhat analogous to Cherenkov radiation is the supersonic shockwave that e.g. airplanes produce when they cross the speed of sound. Cherenkov radiation is always emitted at a fixed angle θ for which:

$$\cos(\theta) = \frac{1}{n\beta}, \tag{2.4}$$

where n is the refractive index of the medium and β is the velocity of the particle relative to the speed of light.

2.1.5 Hadronic interaction

When going through a material, charged hadrons only interact with the electrons of an atom via ionization. However, all hadrons can collide with the nucleus of atoms. When a hadron comes close enough to a nucleus, there is an interaction via the weak forces. I will not describe these in detail, since the interactions are very diverse. Note that since
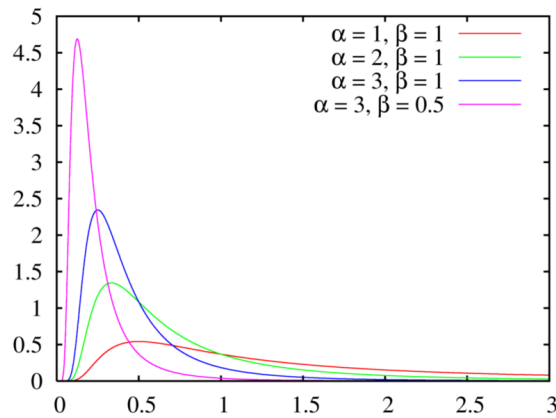
FIGURE 2.5: Some gamma distributions for different parameters α, β

the nucleus of an atom is smaller than the electrons surrounding it the chance for an hadronic interaction is relatively small.

2.1.6 Showers

A particle shower is in fact a cascade of secondary particles produced by an incoming particle going through a medium. These particles are produced by one of the processes mentioned in this section. If a particle has no interactions it just passes through our detector and is called a track. Tracks are mainly hadrons and muons. Each of these secondary particles carries a fraction of the energy of the incoming particle. We call the distance it takes electrons and photons on average to interact with the material the radiation length. For hadrons we call this the interaction length. Electrons and positrons interact with the electron cloud of an atom, while hadrons interact with the much smaller core of the atoms. This results in hadrons having a smaller chance of interacting with the material, and thus a larger interaction length. In the easiest theoretical description each interaction produces one extra particle which carries half the energy of the original particle. In this simple model the energy per particle halves per interaction length. Once the energy of each particle is lower than its critical energy, it can no longer produce new particles. We can calculate the number of radiation lengths it takes for the shower to end:

$$X_{ext} = X_0 \ln(\frac{E_0}{E_c}), \tag{2.5}$$

with X_0 the radiation length, E_0 the starting energy and E_c the critical energy. Note that this is a very basic approximation of the behaviour of a shower. In actuality particles will not always split their energy in half, so showers will not end as abruptly as predicted here. The longitudinal profile of a shower is actually a gamma distribution. Some gamma distributions are displayed in figure 2.5.

In figure 2.6 an example of an electromagnetic shower is displayed. The incoming particle
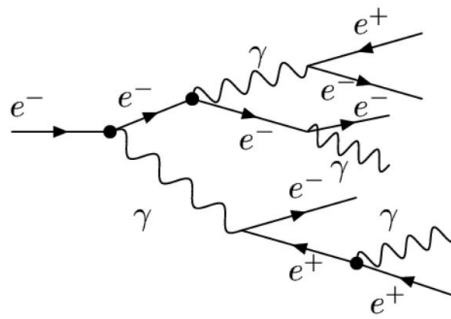
FIGURE 2.6: An example of an electromagnetic shower by bremsstrahlung and pair production

starts by emitting bremsstrahlung, and continues under an angle. The electron then scatters via bremsstrahlung once again while the photon produces an electron-positron pair. The electrons and positron then scatter via bremsstrahlung.

2.2 Scintillator detectors

Scintillator detectors count particles passing through. As a particle passes through a scintillator, it ionizes or excites the atoms in the material. The atoms then proceed to emit a photon. These photons are can only exit the crystal through a photomultiplier. This way all photons eventually pass through the photomultiplier. In the photomultiplier the photons first hit a photo cathode which absorbs the photons, and emits electrons into the electron multiplier.

The electron multiplier consists of dynodes, each at a higher positive voltage than the former, with the lowest voltage near the photo cathode. The electrons are accelerated towards the first dynode due to the electric field. When the electrons hit the first dynode more electrons are produced which are then accelerated towards the second dynode. This process repeats itself until an easily measurable electronic pulse is created at the end of the photomultiplier. This is the signal that is used. The whole process is portrayed in figure 2.7.

Scintillator detectors are used in calorimeters, but also as a particle counter for e.g. triggers or detecting cosmic radiation.
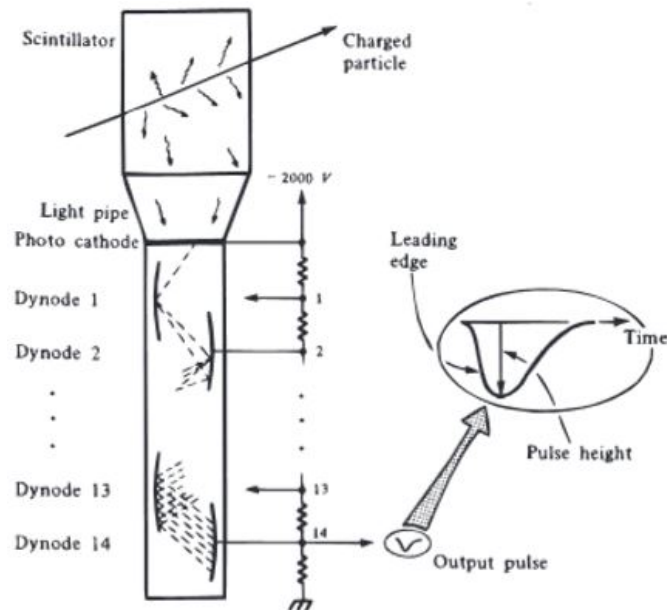
FIGURE 2.7: A schematic drawing of a particle passing through a scintillator [2]

2.3 Calorimeters

Calorimeters are detectors used to measure the energy of particles. This section will explain the different types of calorimeters.

2.3.1 Analog calorimeters

The principle of all calorimeters is to stop a particle in the detector by a stopping material which leads to a shower. The size of the shower is then used to determine the energy of the incoming particle. The first distinction that can be made is between hadronic and electromagnetic calorimeters. Since the hadronic interaction length is longer, hadronic calorimeters need more stopping material and as such a larger calorimeter. In most experiments including ALICE, the electromagnetic is closer to the collision, followed by the hadronic calorimeter. We can also distinguish between homogeneous and sampling calorimeters. Homogeneous calorimeters consist of very heavy scintillators (often a lead-tungsten crystal) that have enough density to stop particles, and can immediately detect them. Sampling calorimeters consist of alternating layers of stopping material (often a heavy metal like lead or tungsten) and sensor and are the most frequent type of calorimeter. Some examples of the sensors used in sampling calorimeters are scintillators or gas chambers. More recently silicon sensors have been used. Silicon is a semiconductor. When a particle passes through the silicon pixel it creates electron-hole pairs which leads to a current. This current is then measured and translated to a digital signal. The downside of the calorimeters mentioned is that they all have a low spatial
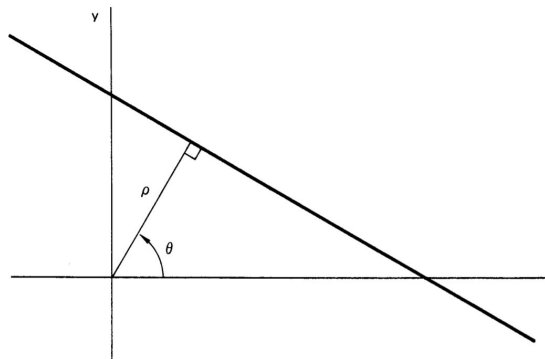
FIGURE 2.8: A visualisation for the parameters ρ, θ in the Hough transform[3]

resolution. This makes it impossible to distinguish between two incoming particles when they arrive close together. For homogeneous calorimeters this resolution is limited by physical constraints. For sampling calorimeters, this can be changed, by changing the detector layers. This is what is done for FoCal.

2.3.2   Digital calorimeters

The FoCal prototype is a different type of sampling calorimeter. In analog calorimeters each sensor measures an amount of particles passing through. In the FoCal and other digital calorimeters, each sensor can only measure a digital signal. The FoCal still consists of alternating layers of metal (tungsten in this case) and detector. However, each layer of detector now consists of separate pixels. Each pixel puts out a signal when a particle passes through it. The energy of the original particle is once again given by the sum of all hits. The benefit of a digital calorimeter is that we can now see the showers progress in the detector. We can trace the incoming particle until it starts showering, and can also easily distinguish between two incoming particles even if they are close together. The disadvantages of digital calorimetry are that it is still expensive, and generates a lot more data than classical calorimeters. The detector used in this experiment is a digital calorimeter made from silicon detectors.

2.4   Hough transform

The Hough transform is a transformation used to easily detect straight lines. We will use it later to find tracks in the detector Through each point in two dimensional space there can be drawn infinitely many lines. These lines can be characterised by two parameters, normally a, b in the function $y = ax + b$. However, we can transform each line to polar coordinates and characterise each line by ρ, θ as displayed in figure 2.8. I will now derive
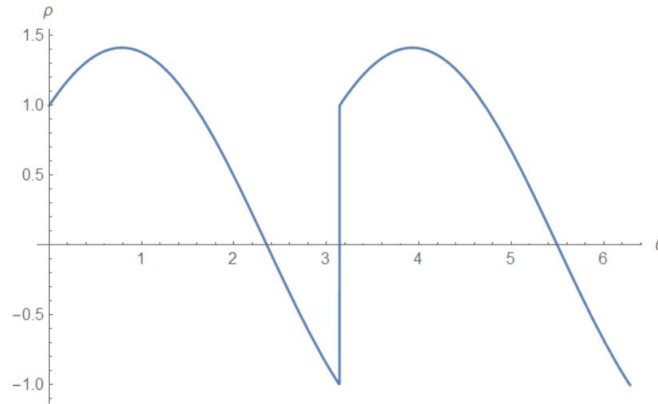
FIGURE 2.9: The Hough transform of the single point $(1, 1)$

a formula for the distance as a function of the point and the angle. The distance between a line $ax + by + c = 0$ and a point (x_0, y_0) is:

$$d(ax + by + c = 0, (x_0, y_0)) = \frac{ax_0 + by_0 + c}{\sqrt{a^2 + b^2}}. \tag{2.6}$$

If we use the equation $y = ax + b$, the relation between a and the angle is: $a = \frac{-1}{\tan(\theta)}$ as the product of two perpendicular slopes has to be -1. We get $y = \frac{-1}{\tan(\theta)} x + c$, which gives $c = y + \frac{x}{\tan(\theta)}$. Since $x_0 = y_0 = 0$ we get the Hough transform as this relation between distance and angle:

$$\rho(x, y, \theta) = \frac{y + x/\tan(\theta)}{\sqrt{1 + 1/\tan(\theta)^2}}. \tag{2.7}$$

In figure 2.9 the Hough transform for the single point $(1, 1)$ is displayed. Since this function has a period of π, the transform will from now on only be displayed on the interval $[0, \pi]$.

Now we have found all possible lines through each point. Logically, if a line goes through two points $\rho(x_1, y_1, \theta)$ and $\rho(x_2, y_2, \theta)$ must intersect. The parameters given at the intersection give the line through both points.

I have displayed the Hough transform for x,z-plane of the whole detector in figure 2.10. The length of the detector is visible at $\theta = 0, \pi$, where ρ ranges from 0 to 10 and 24 different points are visible, these are the layers. At $\theta = \frac{1}{2}\pi$ the width is visible as ρ ranges from -2 tot 2.

In figure 2.11 the Hough transform for the line from one corner of the detector across to the opposing corner is given. Visible here are the 24 lines that represent the Hough transform for each hit per layer. The point where they cross are the parameters of the line through all hits.
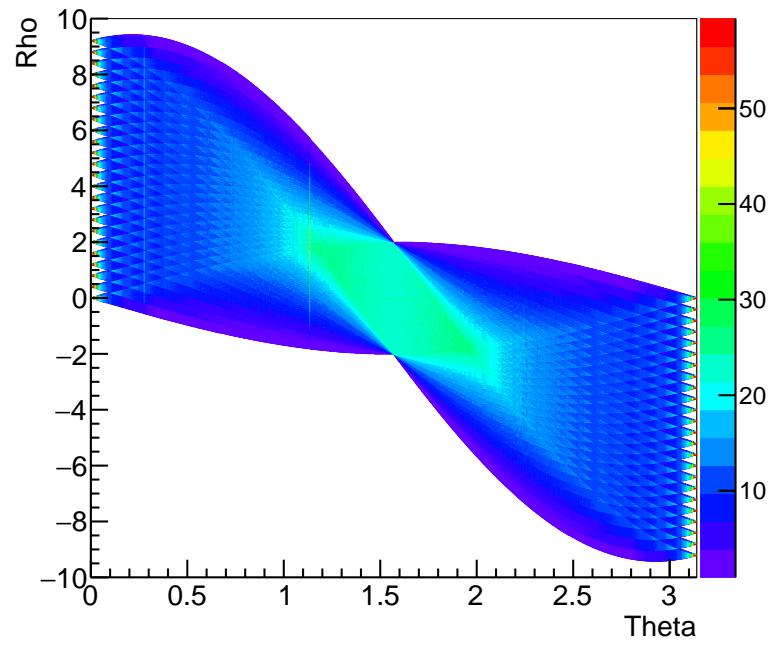
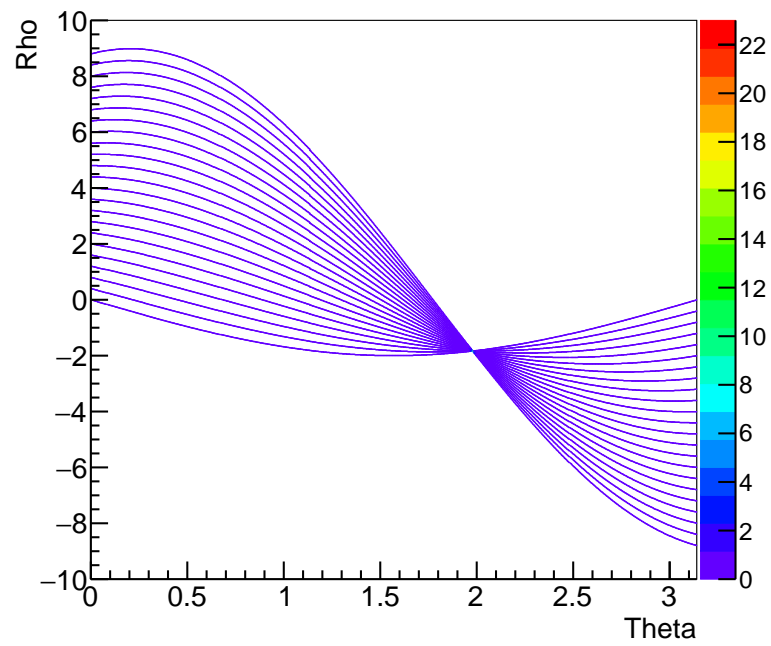FIGURE 2.10: The Hough transform for the full detector

FIGURE 2.11: The Hough transform for the line from (0,-2) to (11,2) in the detector

Chapter 3

The FoCal prototype detector

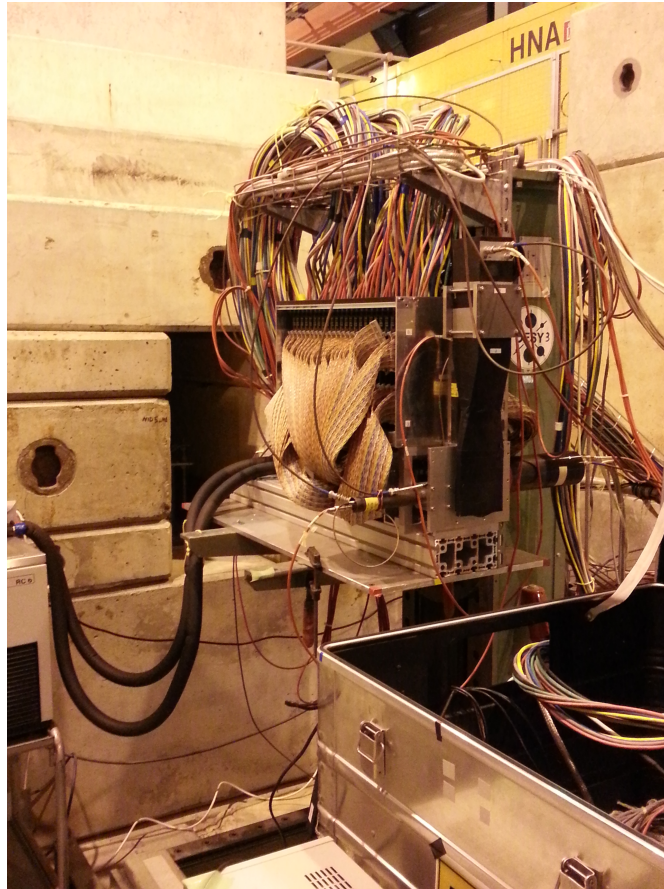In this chapter the FoCal prototype detecor is explained.

3.1 Sensors

The detector uses PHASE II MIMOSA23 Monolithic Active Pixel Sensors (MAPS) chips designed by the Institute Pluridisciplinaire Hubert Curien (IPHC) as sensors. These consist of silicon detectors. When a particle passes through a voltage is created in a single pixel which is then measured. One sensor is 19.52 by 20.93 mm in size with an active area of 19.2 by 19.2 mm, consisting of 30 by 30 μm pixels. This means each sensor contains 640 columns consisting of 640 rows of pixels. The columns are divided into 4 channels, each consisting of 160 columns. A sensor is read out one row at a time, which takes 1 μs, meaning it takes 640 μs to read out a sensor. The full read-out of a sensor is called a frame. Since the sensors are unfortunately not perfect, it is possible for a pixel be on without a particle passing through. There is also a difference in sensitivity per pixel, making some pixels more likely to turn on than others. There are also some broken pixels which are always on and some that are always off. The sensitivity of the sensors can be tuned with 2 parameters, responsible for the signal threshold and the uniform response of lines. These where previously set such that the noise over the detector on average is 10^{-5} per pixel. When a highly energetic particle travels through the detector, it will deposit a relatively large amount of energy in the pixel it passes through. This lead to a high charge in that pixel, which can diffuse into neighbouring pixels. This leads to so-called clusters.

3.2 Layers

To achieve a detector surface of 3.84 by 3.84 cm, each layer of the detector consists of 4 sensors which slightly overlap on the vertical axis to eliminate the edges which have no detectors. This not the case for the horizontal axis. Each sensor is connected to a printed circuit board (PCB). Between each layer of sensors a layer of approximately one radiation length of tungsten is placed. Tungsten is used because it has a small radiation length and it has a small Molière radius. This means that most of the shower's energy deposition happens in that small radius, making it easier to distinguish between showers. There is no tungsten before the first layer. Between layer 21 and 22 there is an additional 6.7 radiation lengths to make sure most of the electromagnetic showers are contained in the detector. The total radiation length of the detector is 28.1 X_0. From now on we will call the horizontal axis of the a layer the x-axis, the vertical axis of a layer the y-axis and the axis into the detector the z-axis. $(0, 0, 0)$ is positioned in the center of the first sensor layer.
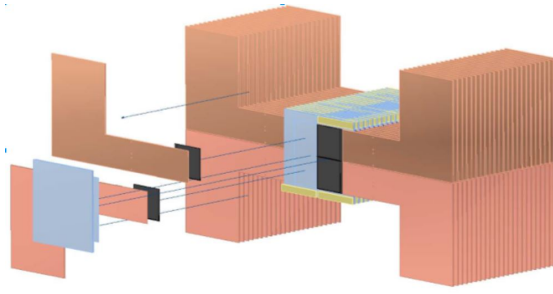
FIGURE 3.2: A schematic drawing of the sensors, tungsten and PCB that make up the detector

3.3 Scintillators

Since the detector cannot constantly take data, a trigger to determine when a particle passes through the detector is needed. In the case of the 244 GeV data, the scintillators used for these triggers are Presence (P), Front (F), Horizontal (H), Vertical (V) and Back (B). They are positioned as visible in figure 3.3. The Presence is 11x11 cm, the Front is 4x4 cm, both the horizontal and vertical are 2x1 cm and their overlap is positioned exactly over the middle of the detector and the back is 4x4 cm and positioned at the end of the detector. Each scintillator has noise, so using only one as a trigger would give
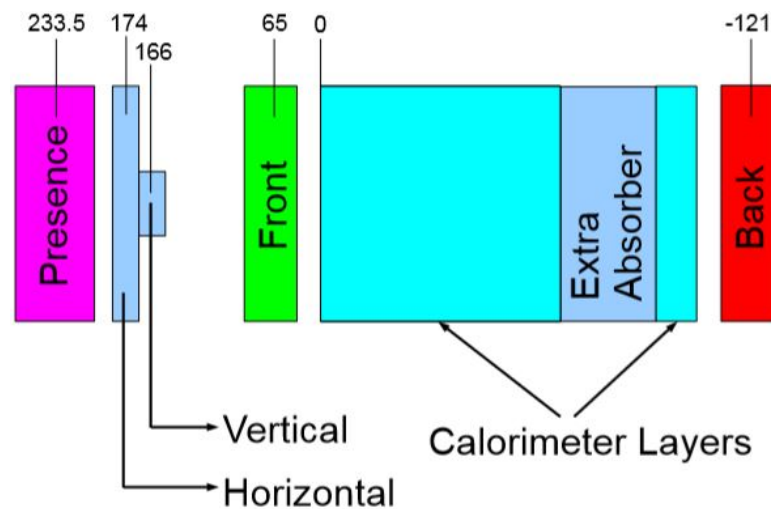

FIGURE 3.3: A not to scale schematic drawing of the trigger scintillators and their position [4]

a lot of empty frames due to fake triggers. That is why the coincidence of two or three scintillators is used to establish a signal. The combinations are PF, HVF, BF and HF. HF is never used since it is just a check for the HVF.

3.4 Cooling

Each sensor produces around 450 mW of heat, meaning the full detector produces well over 40 W of heat. This will lead to the detector significantly warming up unless cooled. An increase in temperature leads to more thermal noise, which leads to a less clear signal, so it is imperative that the detector is cooled. To achieve this the sensors and tungsten are connected to heat sinks, which are subsequently cooled by water from a reservoir at 17 °C. The cooling system succeeds in keeping the detector around 27 °C.

3.5 Data acquisition system

The data from 6 layers is transferred from the PCB's to a Spartan chip (FPGA integrated circuit) which regulate the timing of the read-out. From the Spartan chip it is then transferred to a memory buffer. This is done in two Virtex boxes, each containing one memory buffer, two Spartan chips and a Virtex FPGA which handles buffering and communication with the data acquisition computer (DAQ). Once the buffer is full and the whole detector has been read out, the data is transferred to the DAQ which takes about two minutes in which no new data can be taken.

Chapter 4

Data processing

In this chapter I will explain how data (specifically the 244 GeV data), are processed and made ready to be used for analysis.

4.1 Demultiplexing

The first step in data processing is demultiplexing. In this process, the raw data as received by the DAQ computer is first separated into different channels. The data is then matched to the corresponding pixels in each channel. Afterwards the data from different channels is aligned. Lastly the sensor multiplexing is removed, and the data is written in a usable format.

4.2 Pedestal runs

The next step is to use the pedestal runs. Pedestal runs are runs consisting of frames taken when there is no beam passing through the detector. Pedestal runs consist only of noise. A distribution is then made of all pixels as a function of the fraction of time the pixel was active, as visble in figure 4.1. The most active pixels are deleted from the data until an average noise of 10^{-5} is reached. These pixels will also be deleted from the runs with beam. The deleted pixels consist of broken pixels that are always on, and pixels that just have to much noise. In figure 4.2 an example of the effect of applying the pedestal data is displayed.
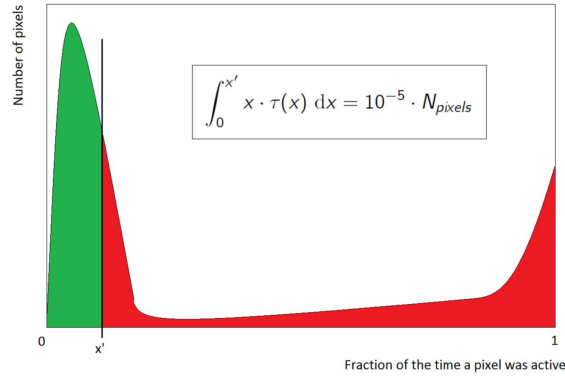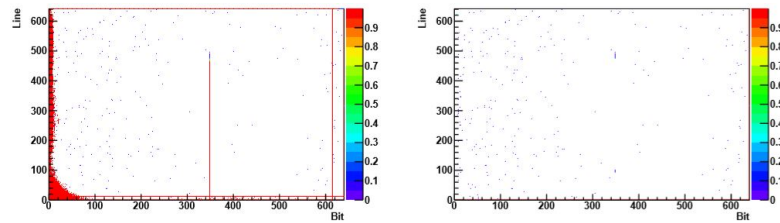
FIGURE 4.1: An example of a possible noise distribution for all pixels [5]

FIGURE 4.2: A single chip before and after applying the noise level of 10^{-5} [5]

4.3 Malfunctions

Unfortunately some chips and some channels are badly damaged and always on, while others are completely unresponsive. Other channels have too many hot lines (column that is always on) so that it is impossible to read out actual data from that channel. Because of this, these chips and channels are masked completely in the data, and will not be used in further analysis. I have displayed the hit maps for all 244 GeV runs combined in figure 4.3. In this figure the different sensitivities of each sensor are clearly visible. The right bottom chip in layer 10 for example, displays a significantly smaller number of hits than the other chips in the same layer. Also visible are which channels and chips have been excluded from the data.
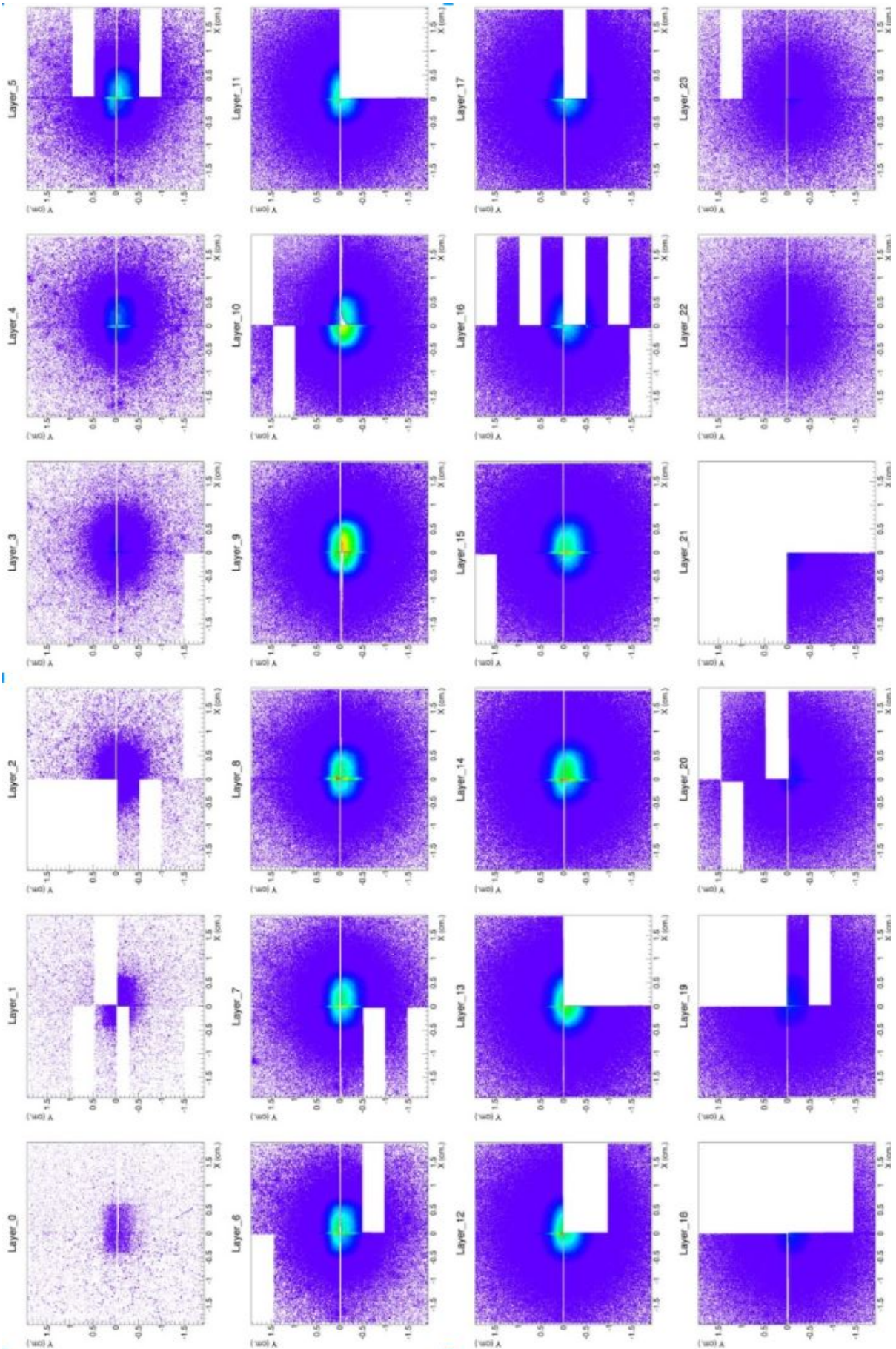
FIGURE 4.3: An overview of all chips

Chapter 5

Data analysis

In this chapter all parts of my research will be discussed. The data consist of 27 runs (run 30-56) including pedestals, all at an energy of 244 GeV. The data used is uncalibrated.

5.1 Trigger Analysis

Because the 244 GeV data contain a mix of both electrons and hadrons, consisting mostly of pions and protons, I attempted to separate the frames with electrons from the frames with hadrons via the trigger data. Since electron-showers are almost always fully contained in the detector and hadrons either leave tracks or start showering later in the detector, If a particle leaves the detector (and as a consequence the back scintillator is triggered) the incoming particle will most likely have been a hadron. I have displayed

TABLE 5.1: An overview of all triggers and their respective frequency

Name	Abbreviation	Frequency of triggers
Horizontal Front	HF	10976
Back Front	BF	9516
Front Presence	FP	16798
Horizontal Vertical Front	HVF	7763
Spill	None	17029

the frequency of triggers in Table 5.1. The interesting trigger for the selection of hadrons is the BF, since it includes the back scintillator. This means that the distribution of the total hits per frame for all events for the BF trigger should look different from the HVF trigger hits distribution. I have displayed the hits distribution for HVF and BF in figure 5.1 and 5.2. The hits distribution can be divided into roughly three parts. From 0 to 1000 hits we have the noise peak, combined with the track peak. From 1000 to 40000 hits we have a gradually decreasing slope, which are the partial showers. This region
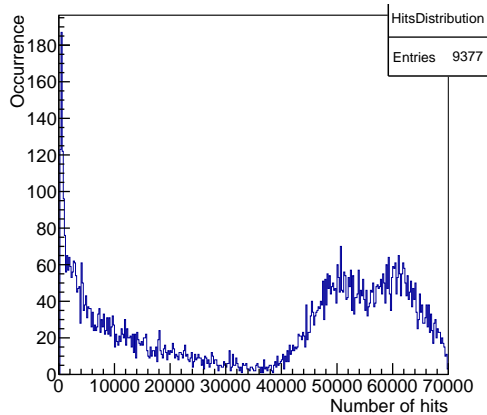
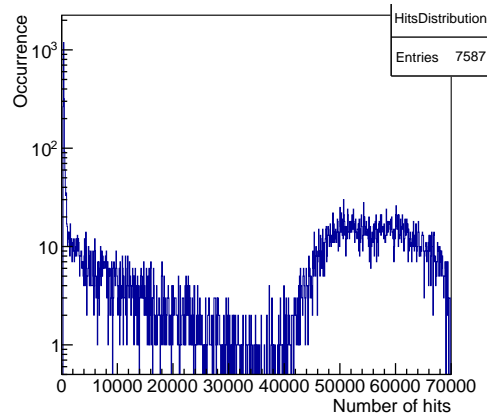FIGURE 5.1: The distribution of all hits per frame for the BF trigger

FIGURE 5.2: The distribution of all hits per frame for the HVF trigger

is very large, because it mostly hadrons with only a few interactions in the detector as well as hadrons that shower almost completely. The last region is 40000 to 75000 hits and contains all full showers which are mainly electrons.

Now for the BF distribution, we would expect a decrease in full showers, so the peak at 55000 should be smaller with regard to the HVF distribution. Unfortunately, the full energy peak is about a third of the noise peak for BF, while it is $\frac{1}{500}$ for the HVF. There appear to be more electrons in the BF triggers than in the HVF triggers. The most likely explanation for this behaviour is that the Back scintillator is not working properly. This problem was noticed in earlier experiments and is not completely unexpected. Because of the lower sensitivity of the back scintillator single tracks do not always trigger it, while remnants of full showers do because it is a stronger signal.

From this point on I will constantly use the HVF trigger to select events as it gives all central events. These events give showers that are best contained in the detector, and thus are measured best. Because the separation of particle types via trigger did not work out as hoped, from now on particles will be separated based on the division shown in table 5.2.

TABLE 5.2: The division of all events by hits per frame

Tracks	0-1000 hits	6884 events
Partial showers	1000-40000 hits	3487 events
Full showers	40000-70000 hits	6271 events

This division is based on the hits distribution in figure 5.2. The peak from 0-1000 hits are all the tracks and empty frames. Then From 1000-40000 hits we have a slowly decreasing slope which are the partially developed showers. These showers either stop showering before depositing their full energy, or leave the detector before depositing

their full energy. Partial showers consist mostly of hadronic showers. Around 40000 hits the frequency of events increases, and we get to the full energy peak. These are all showers that deposit their full energy in the detector. Since electrons always shower in the detector, they almost always deposit their full energy. This means that the full showers are mostly electrons.

5.2 Longitudinal profiles

In order to characterise different showers I looked at the longitudinal profile of individual frames in the detector. I have included a few examples in figure 5.3, 5.4 and 5.5. As
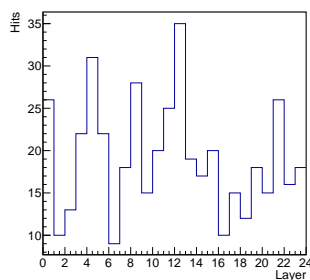
FIGURE 5.3: Longitudinal profile of a track
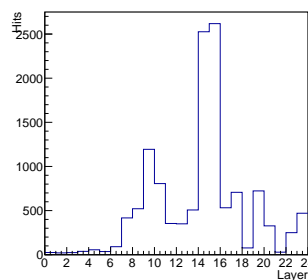
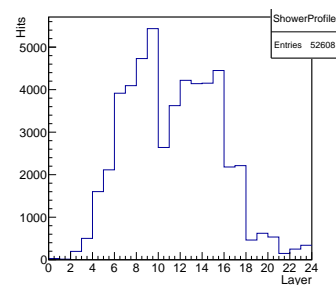FIGURE 5.4: Longitudinal profile of a partial shower

FIGURE 5.5: Longitudinal profile of a full shower

expected, for the full showers we see a peak and then a steady decline in hits per layer. The track events do not have enough hits per layer to significantly rise above the noise and their longitudinal profiles are indistinguishable from empty frames. partial showers are distinguishable from full showers because both the peak and the start of the shower is deeper into the detector. The goal of this subsection is to find a function for shower lengths.

5.2.1 Shower start point

First it is necessary to define the start point of a shower. The average noise level in a layer is $640 \cdot 640 * 10^{-5} \approx 40$ hits, so I chose an arbitrary level of 100 hits as a strong enough signal to indicate a shower. The start point of a shower is then defined as the first of two consecutive layers which both have 100 or more hits. I also allowed for one layer of less then 100 hits in between. If we then divide the events into the three categories we get the distributions as in 5.6, 5.7 and 5.8.

It is clearly visible that for the full showers the start points are in the first few layers. According to theory an exponential distribution should be visible. This distribution is
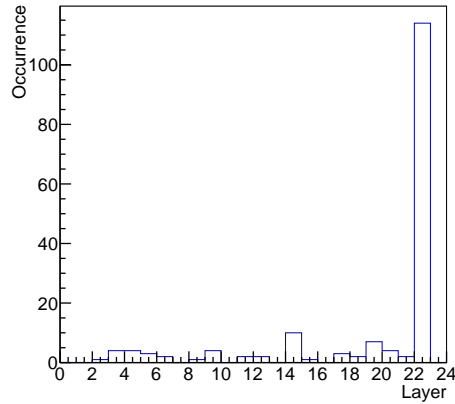
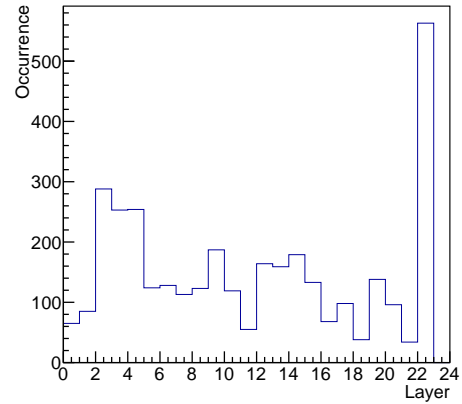FIGURE 5.6: Histogram of start
points per layer for tracks

FIGURE 5.7: Histogram of start
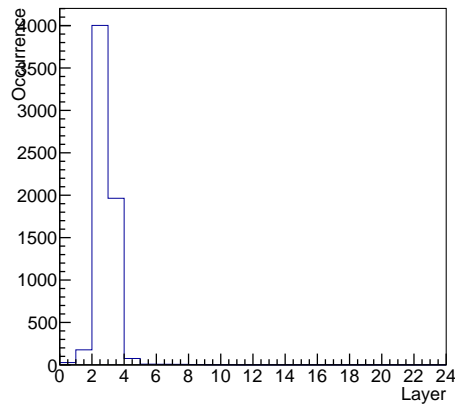points per layer for partial showers

FIGURE 5.8: Histogram of start
points per layer for full showers

visible with the exception that layer 1 is much lower than layer 2. This is probably because it is very hard to have 100 hits in layer 1 even if the shower has already started by then. The start points for partial showers are distributed more evenly across the detector. This is as expected, since the detector is only one interaction length for hadrons. The fluctuations in the distribution are probably due to the fact that this is uncalibrated data, and all layers have different sensitivities. I have displayed the start points for the tracks. Because tracks have a low number of hits, only a small number of start points are found. This is as expected, since the tracks should not shower. For both the tracks and the partial showers there is a peak in layer 22. This is probably due to the fact that there is a thick block of tungsten before this layer. More showers will start in this block leading to a lot of hits in layer 22.

5.2.2 Shower end point

Now that we have a start point we now try to define an end for the shower. This is a very hard task since showers do not have a clear end. If all energies were distributed symmetrically in interaction in the detector all particles should fall under the critical energy in the same layer. In reality this is not the case and showers have a long 'tail' which makes it hard to define an end. At first, the end point was defined as the first of three consecutive layers for which the number of hits is less than 100 hits. This gave very few end points. In varying this value I found either not enough end points or very broad distributions of end points. To solve this the number of hits of the layer after the start point is used as threshold. So if the start point is layer 1, we use the number of hits in layer 2 in the definition for end point. The end point is defined as the first of three consecutive layers where the hits per layer is less than the threshold. If we now
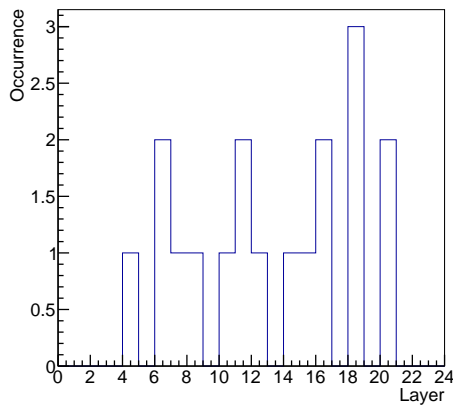

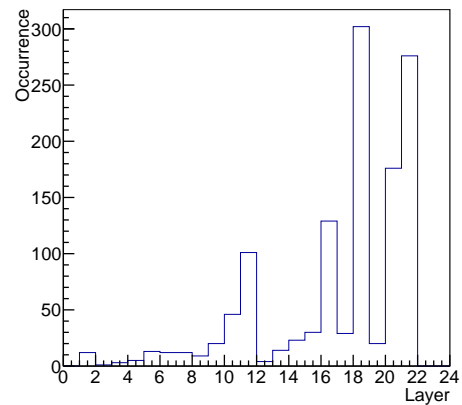FIGURE 5.9: Histogram of end points per layer for tracks

FIGURE 5.10: Histogram of end points per layer for partial showers
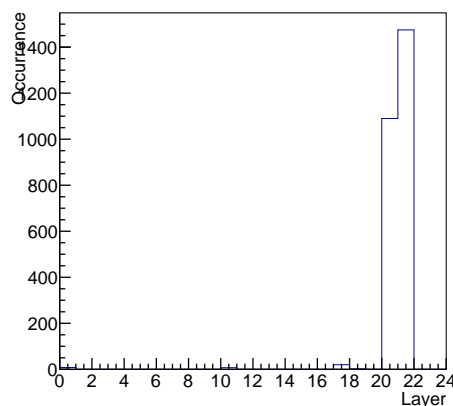

FIGURE 5.11: Histogram of end points per layer for full showers

look at the distributions of end points as in figure 5.9, 5.10 and 5.11, we see that the full showers all end around layer 20 and 21. The fluctuations in the distribution are again

due to the fact that this is uncalibrated data. For the partial showers we once again see a more even distribution of end points, as some showers end before having deposited their full energy in the detector.

5.2.3 Shower length

We can now find the three distributions for shower lengths by subtracting the end points from their respective start points. I have displayed the hadron tracks as well, even though there are not enough entries to actually conclude something. For the full showers we see a distribution around a length of 18 layers. And for partial showers we once again have a much broader distribution, even though there is once again a peak around the length of 18 layers.
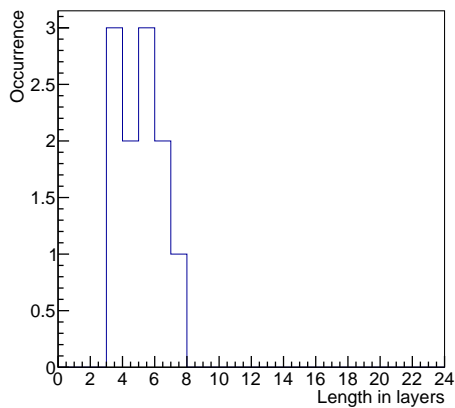

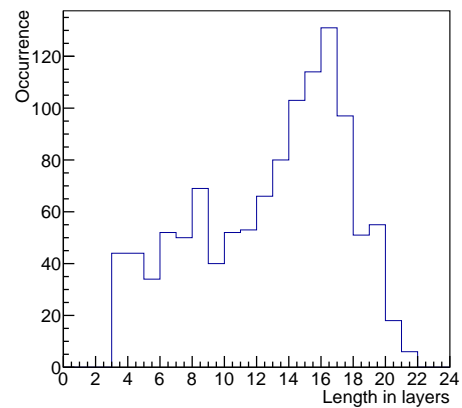FIGURE 5.12: Histogram of shower lengths for tracks

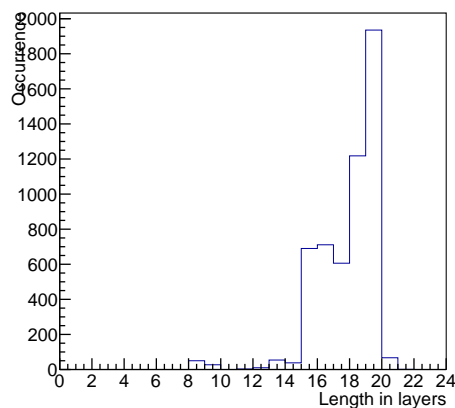FIGURE 5.13: Histogram of shower lengths for partial showers

FIGURE 5.14: Histogram of shower lengths for full showers

5.2.4 Efficiency longitudinal analysis

In this subsection I want to discuss the efficiency of the criteria I used to find the length of showers. In table 5.3, the number of events and start and end points per type of event is visible. It is clear that the effectiveness for tracks is very low. This was to be expected, as these tracks should not show strong showers. For the partial and full showers the effectiveness of finding the start point is close to 100%. This means that the method used for finding the start points is a reliable method. The end points have an efficiency of $\approx 35\%$ for partial showers and $\approx 85\%$ for full showers. Since partial showers do not deposit their full energy in the detector, it is logical that we often cannot find an end point. The method is very reliable for full showers.

TABLE 5.3: A table of the number of found start and end points compared to the number of events

	total events	found start points	found end points
Tracks	6884	160	18
Partial showers	3487	3464	1237
Full showers	6272	6272	5410

5.3 The Hough transform

As an alternative for the track finding algorithm that is already used and mainly with the goal to find secondary tracks, the Hough transform was implemented. This was inspired by this article [6], which did the same for hadronic showers in a different calorimeter. The article suggested it was not necessary to implement the Hough transform in three dimensions and either the z,x or z,y plane would suffice. As stated in section 2.4, the Hough transform is given by the following relation between radius, angle and position: $\rho(x, y, \theta) = \frac{x + y / \tan(\theta)}{\sqrt{1 + 1 / \tan(\theta)^2}}$ I tried both a Hough transform using only clusters and with all hits. I found that using all hits presents a clearer image than using only clusters. For this section the so-called past-future protection is turned off, allowing for multiple incoming particles per frame.

5.3.1 Implementing the Hough transform

In implementing the Hough transform, the bin size matters. If the bin size is too small, the transforms of each point in the detector will not intersect, and we will not find a distinct peak. However, if the bin size is to large we will not have enough accuracy.

After trying various bin sizes, I used 1000 bins for the angle and 500 for the radius. In figures 5.15 and 5.16 I have displayed the hough transformed datas for a double track and a shower. To acquaint the reader with the Hough transform and with interpreting Hough transformed data, more examples and explanation can be found in appendix A
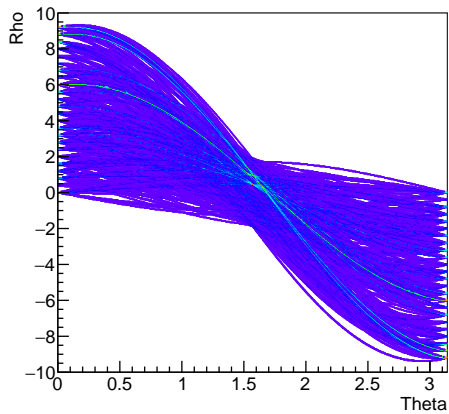

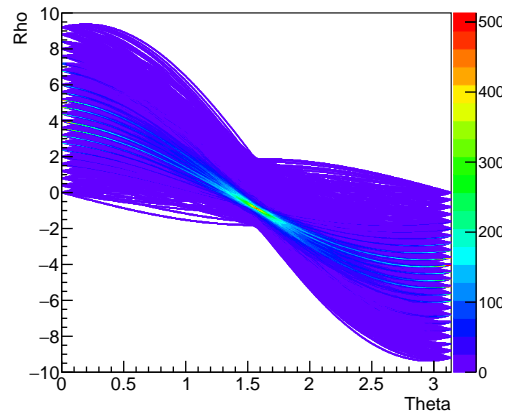FIGURE 5.15: The hough transformed data of two tracks

FIGURE 5.16: The hough transformed data of a shower

For the displayed events we can clearly see a peak around $\frac{1}{2}\pi$. Since we look at the z,x plane this is the path straight through the detector. Note that it is hard to distinguish the partial and full showers from each other. One way we can distinguish them is to look at which layers contribute the most to the distribution. In this thesis, the value of the peaks in the hough transformed data is not used for analysis. This might be another way to distinguish between partial and full showers.

5.3.2 Finding tracks

The next step is to read out the maxima of the hough transformed data and draw these lines through a two dimensional map of the hits. The lines are drawn from layer 0 to layer 23 and are drawn with the following formulas:

$$x_0 = \rho(\sin(\theta) + \frac{\cos(\theta)^2}{\sin(\theta)}), \tag{5.1}$$

$$x_{23} = \frac{-1}{\tan(\theta)} * 11 + \rho(\sin(\theta) + \frac{\cos(\theta)^2}{\sin(\theta)}), \tag{5.2}$$

with x_0, x_{23} respectively the x-coordinate in layer 0 and 23 and ρ, θ the maxima read out from the histogram. In order to be able to find multiple tracks, I took the three highest maxima from the Hough transformed data. Since showers have widely distributed maxima, I also required that each maximum be at least 10 bins apart in the θ direction and

5 in the ρ direction (in both cases 1% of the total number of bins). In figure 5.17, 5.18 and 5.19 are three events to which I have applied this procedure. The procedure clearly
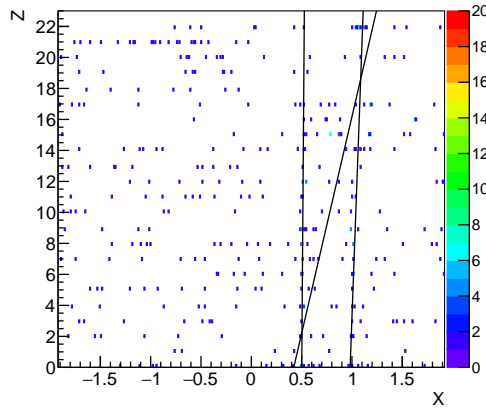

FIGURE 5.17: Histogram of the x,z plane of a double track with found tracks
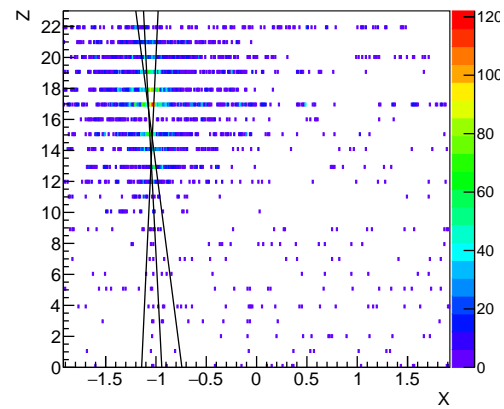

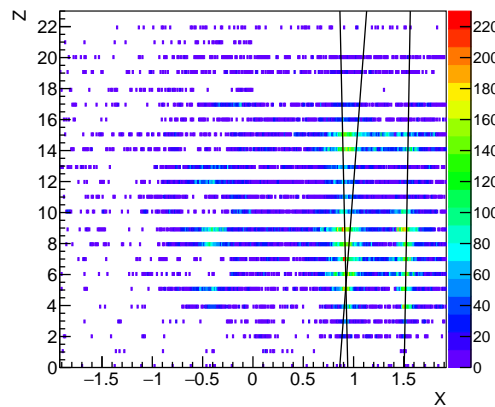FIGURE 5.18: Histogram of the x,z plane of a partial shower with found tracks

FIGURE 5.19: Histogram of the x,z plane of a full shower with found tracks

succeeds in finding the track of the incoming particles. The accuracy of the line is bigger when looking at tracks or partial showers with a low amount of hits since the shower overshadows the track in the Hough transform. Unfortunately, the track event displayed here has a secondary track that is not found via this method. The third line is through an arbitrary number of points that happen to line up. In the shower events there are no secondary tracks, and the other lines are part of the same maximum in the hough transformed data. The angle between these lines is dictated by the requirement that the maxima be respectively 10 and 5 pixels apart. In conclusion, the two dimensional Hough transform presents a different way to find the incoming particle. It does not succeed at finding secondary tracks. This easiest way to solve this might be to implement the Hough transform in three dimensions, or try the Hough transform with clusters. Both
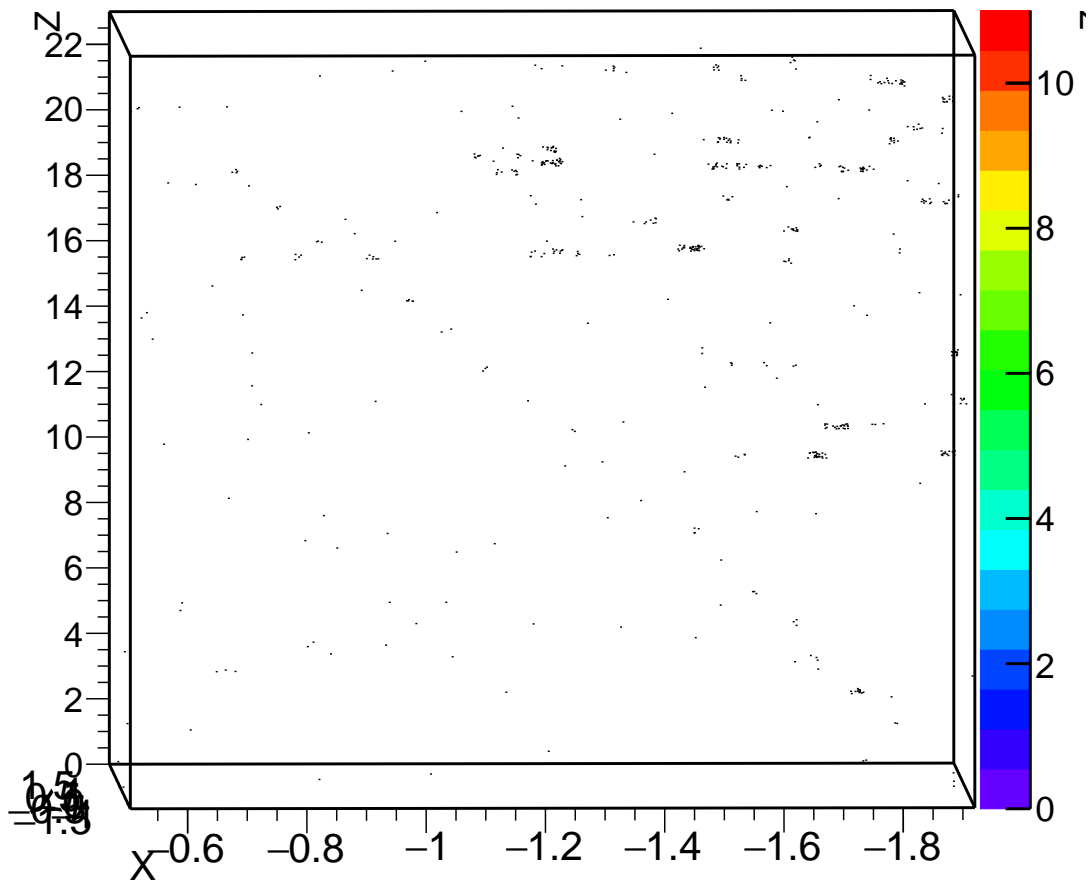
FIGURE 5.20: The event discussed in section 5.4, zoomed in on the x-axis

of these ways reduce the noise and lead to a stronger signal. Another way might be to select maxima in a different way.

5.4 Interesting event

While looking at individual events, I came across a rather interesting event which I will discuss here. In run 55 the first event is a track of a particle that enters the detector at $(-2, -0.3)$ and in layer 18 is at $(-0.7, -0.9)$, as can been seen in image above. Layer 18 is at a depth of 73,7 mm, which means the particle makes an angle of $\arctan(\frac{2-0.7}{7.37}) \approx 10^o$. With this angle and point of entry, it is impossible for the particle to have hit the Front scintillator since this has the same size as the front of the detector and is a few centimeters removed from the detector, it can have gone through the Presence scintillator. The particle can have gone through the perspex part of the Front scintillator however. When passing through, it will not produce photons the normal way,

but can produce Cherenkov radiation. This Cherenkov radiation might have triggered the photo multiplier and resulted in a signal. So theoretically it is possible for the Front scintillator to have been triggered by the Cherenkov radiation, but it does seem very unlikely.

The question remains where this particle originated. It cannot have come from the beam, since it has too large of an angle. The particle cannot come from cosmic radiation, since it moves almost horizontally. This leaves other experiments from the same hall. The problem is that the experiment was conducted at the edge of the hall and there were no neighbouring experiments from the side the particle came from.

So in conclusion, even though we have a (albeit unlikely) explanation for the trigger, it is unclear from where this particle originated.

Chapter 6

Conclusions and recommendations

In this thesis, I have analysed 244 GeV SPS data taken with the FoCal prototype detector. I have analysed the triggers, and tried to separate the incoming hadrons from the electrons via the back scintillator. I found that the Back scintillator is not functioning properly, and instead of selecting less electrons and positrons it selects more. If this problem is fixed before future beam tests, one might be able to separate electron and hadron data with it. Because the scintillator was not functional for this data, it is still unclear whether that would work.

Because this seperation does not work, the showers are categorised as in table 5.2. Note that this is a very rudimentary division.

After that the longitudinal profile of the showers was analysed. A definition for starting and ending point was made, giving the ability to calculate the length of showers. This gave a narrow distribution around a length of 18 layers for full showers, and a broader distribution around 16 layers for partial showers. This is not enough difference to distinguish showers from eachother. There is a clear difference between the starting points, and we can say that if a particle starts showering after layer 4 it is most likely not an electron or positron. The definitions for starting and ending point in the longitudinal analysis are somewhat arbitrary. It might be possible to refine these definitions, resulting in a clearer difference between partial and full showers.

Implementing the Hough transform was done successfully, and the result were promising. Via the Hough transform I was able to consistently find the track of the incoming particles. The real goal was to find secondary tracks, this was not succesful. The difficulties originated from the fact that the signal of secondary tracks in the Hough transform was not strong enough. However, there were also difficulties finding enough

events with secondary tracks. In the future, it might be useful to test the Hough transform with simulated data before implementing it with real data. In this thesis only the two-dimensional Hough transform was used. This may have led to the problems with finding secondary tracks. In a three dimensional Hough transform the signal remains as strong, while the noise is spread over a second dimension. I was unable to finish implementing this, but maybe further research can look into this.

Then finally I looked into the strange event of a particle going diagonally through the detector. Although I have not been able to explain this event, no other such events were found making it not very significant.

Appendix A

Examples of Hough transformed data

In the figures on the next pages I have displayed the Hough transformed data for six frames. Figure A.5 and A.6 are also used in chapter 5. Since θ is the angle of the line perpendicular to the track and we work in the z,x plane, $\theta = \frac{1}{2}\pi$ is the path straight through the detector. It is possible to distinguish individual layers by looking at the left and right edges of the histogram. There are 24 points where the functions begin, one for each layer. the earlier layers are the ones closer to zero. This allows us to see which layers contribute most to the distribution, and thus are near the shower maximum. In figure A.6 and A.4 the middle layers contribute most so this is probably an electromagnetic shower. In figure A.2 the later contribute most, so this is most likely an hadronic shower. Figure A.1 gives a maximum that is slightly away from $\frac{1}{2}\pi$ and is the shower of a particle that entered the detector under an angle. Figure A.3 and A.5 have small maxima, so these are hough transforms of tracks.
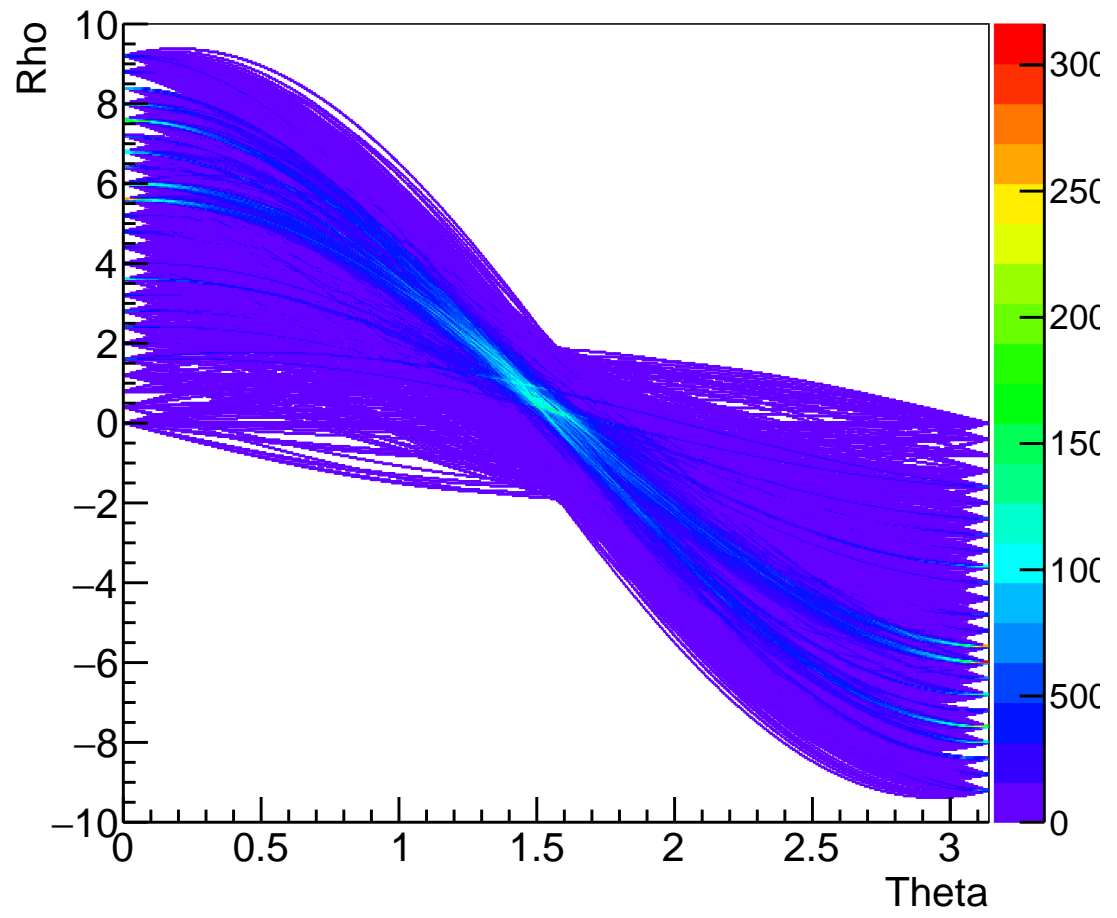
FIGURE A.1: The Hough transformed data for run 32 frame 158
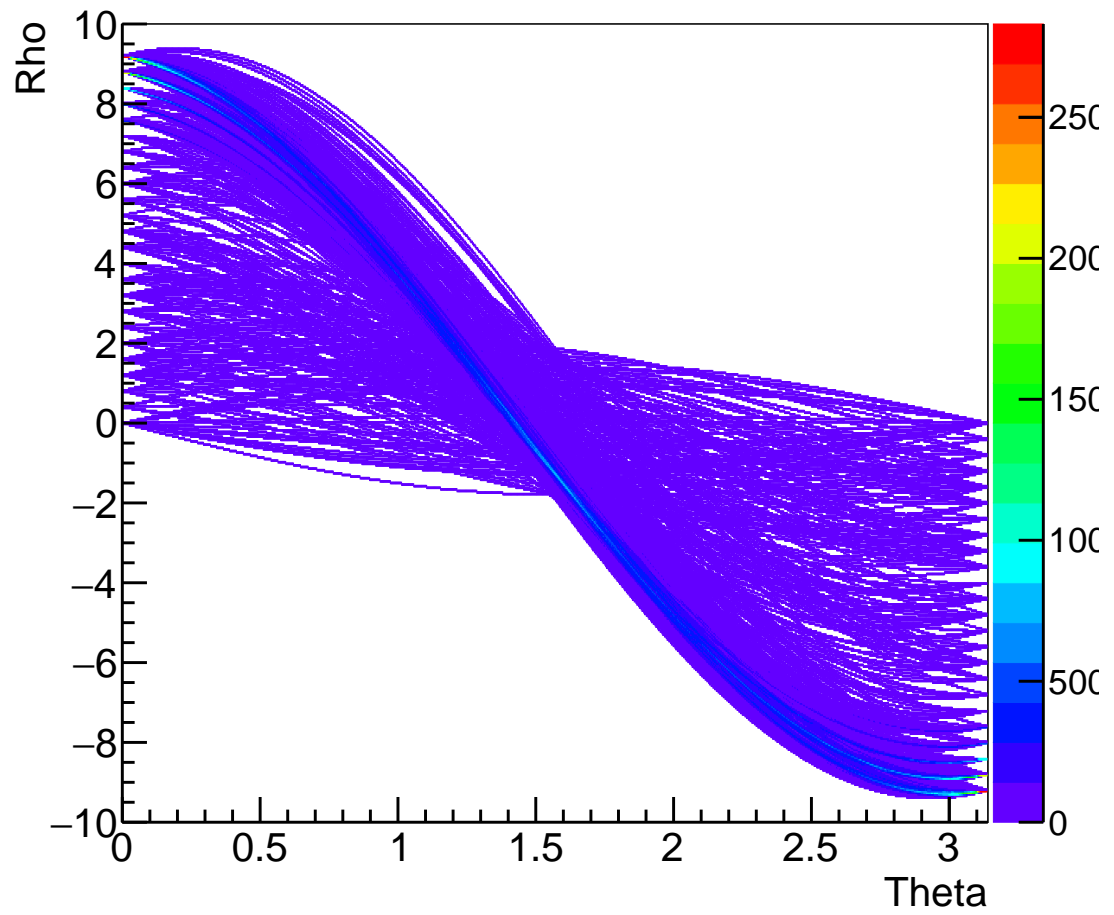
FIGURE A.2: The Hough transformed data for run 32 frame 970
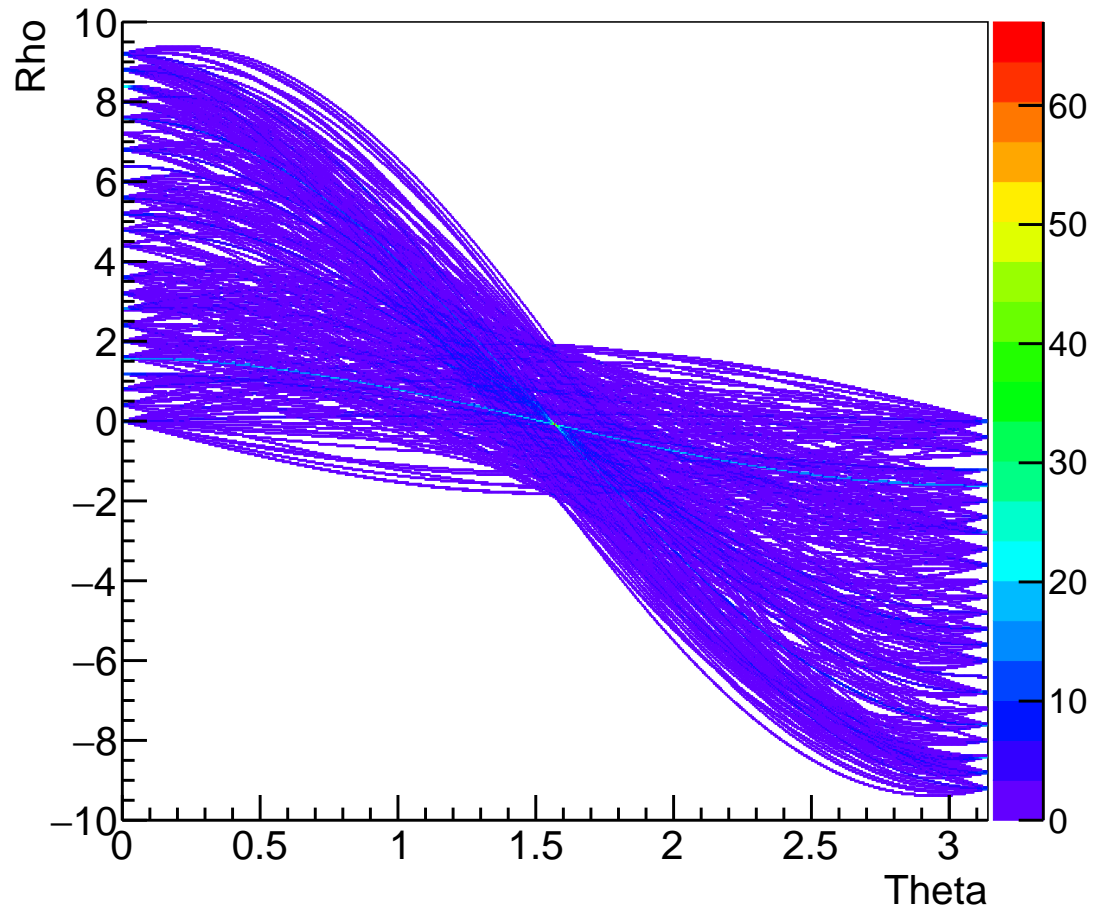
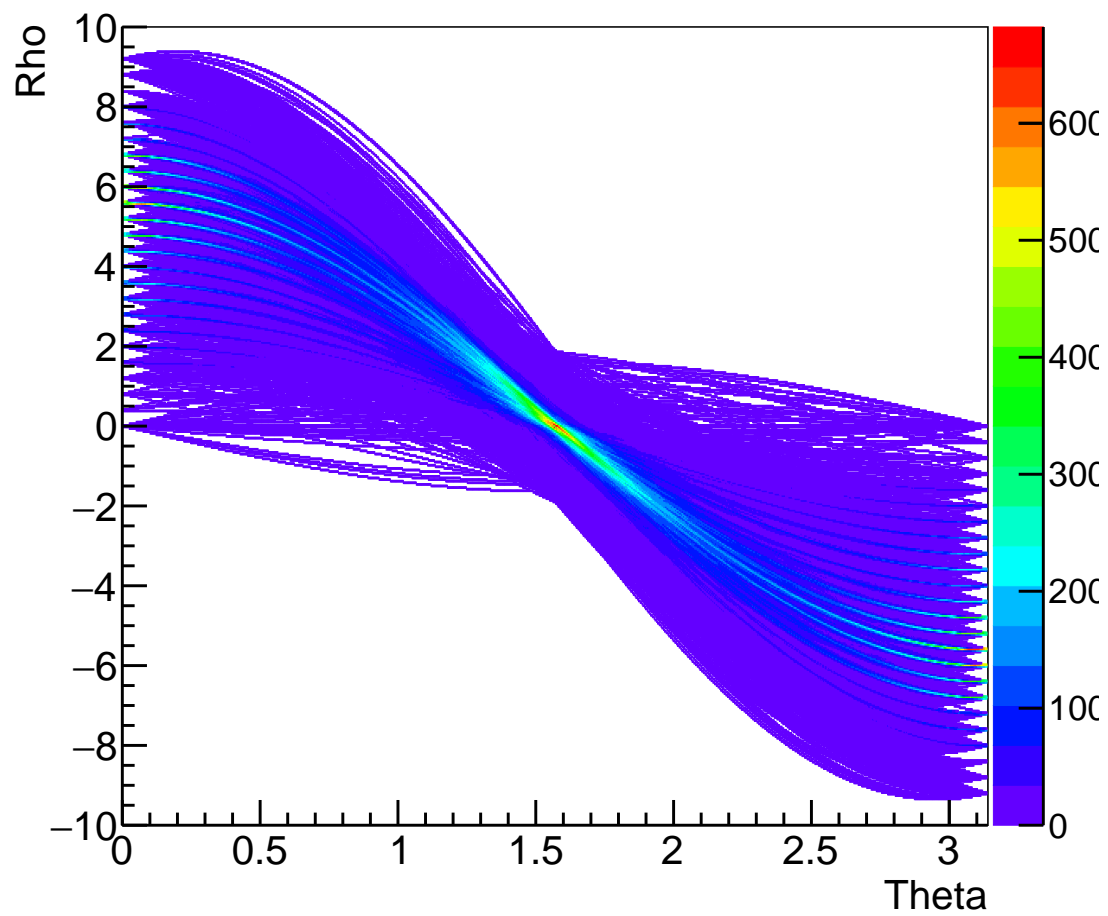FIGURE A.3: The Hough transformed data for run 42 frame 970

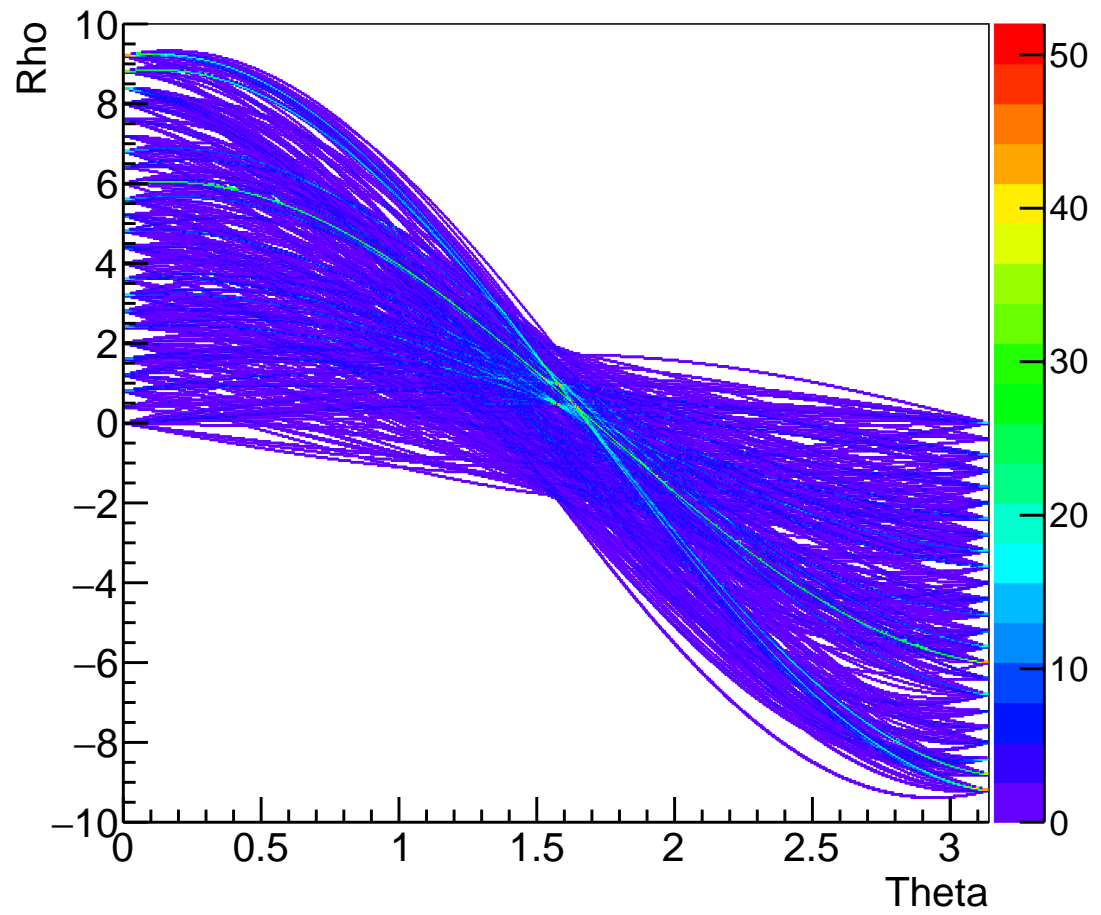FIGURE A.4: The Hough transformed data for run 47 frame 504

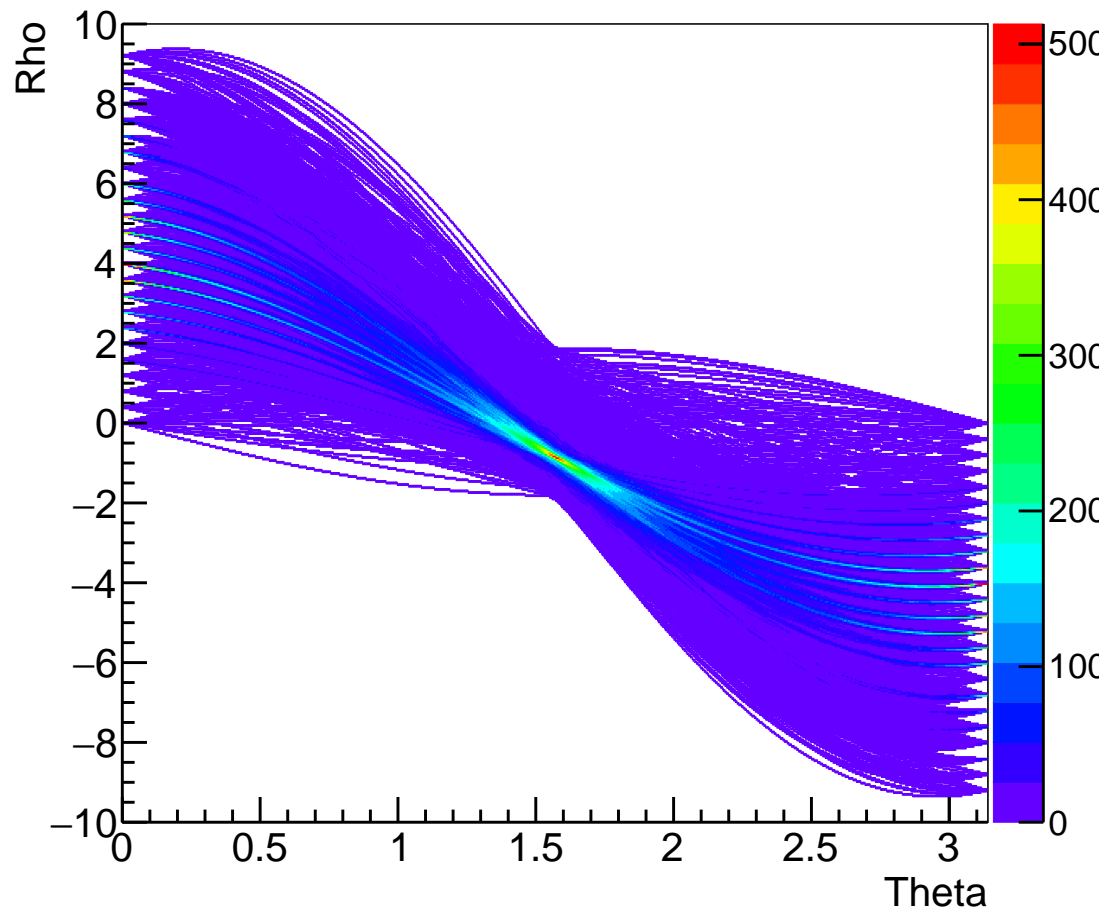FIGURE A.5: The Hough transformed data for run 55 frame 279

FIGURE A.6: The Hough transformed data for run 55 frame 561

Bibliography

[1] S.R. Klein H. Bichel, D.E. Groom. *Passage of particles through matter*. Particle data group, 2012.

[2] Alejandro Garcia Ernest M Henley. *Subatomic physics*. World scientific, 3 edition, 2007.

[3] Peter E. Hart Richard O. Duda. Use of the hough transformation to detect lines and curves in pictures. *Comm. ACM*, pages 11–15, 1971.

[4] Martijn Reicher. *Digital calorimetry using pixel sensors*. PhD thesis, University Utrecht, 2016.

[5] M. Dietze. Performance study of the focal prototype detector using a 2.0 - 5.4 gev pure positron beam. June 2014.

[6] The CALICE collaboration. Tracking within hadronic showers in the calice sdhcal prototype using a hough transform technique. *Journal of Instrumentation*, 2017.